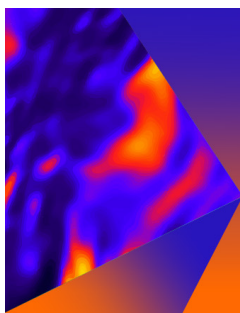# Emergent quasi-two-dimensional ferromagnetic state with perpendicular magnetic anisotropy at La$_{0.7}$Sr$_{0.3}$MnO$_3$/SrCuO$_2$ interface ⓕ⊘

Wenxiao Shi ⓘ ; Jing Zhang ⓘ ; Xiaozhi Zhan ⓘ ; Jialiang Li ⓘ ; Zhe Li ; Jie Zheng ⓘ ; Mengqin Wang ⓘ ;
Jine Zhang; Hui Zhang ⓘ ; Tao Zhu ⓘ ; Yunzhong Chen ⓘ ; Fengxia Hu ⓘ ; Baogen Shen;
Yuansha Chen ✉ ⓘ ; Jirong Sun ✉ ⓘ

Check for updates

View Online   Export Citation

20 June 2024 09:12:49

Emergent quasi-two-dimensional ferromagnetic state with perpendicular magnetic anisotropy at La$_{0.7}$Sr$_{0.3}$MnO$_3$/SrCuO$_2$ interface Ⓕ

Wenxiao Shi,[1,2] ⒾⒹ Jing Zhang,[3] ⒾⒹ Xiaozhi Zhan,[4] ⒾⒹ Jialiang Li,[4] ⒾⒹ Zhe Li,[1,2] Jie Zheng,[1,2] ⒾⒹ Mengqin Wang,[1,2] ⒾⒹ Jine Zhang,[5] Hui Zhang,[5] Tao Zhu,[1,4] ⒾⒹ Yunzhong Chen,[1,2] ⒾⒹ Fengxia Hu,[1,2] ⒾⒹ Baogen Shen,[1,2,6] Yuansha Chen,[1,2,a)] ⒾⒹ and Jirong Sun[1,2,7,a)] ⒾⒹ

AFFILIATIONS

[1]Beijing National Laboratory for Condensed Matter Physics and Institute of Physics, Chinese Academy of Sciences, Beijing 100190, China
[2]School of Physical Sciences, University of Chinese Academy of Sciences, Beijing 100049, China
[3]Songshan Lake Materials Laboratory, Dongguan, Guangdong 523808, China
[4]Spallation Neutron Source Science Center, Dongguan, Guangdong 523803, China
[5]School of Integrated Circuit Science and Engineering, Beihang University, Beijing 100191, China
[6]Ningbo Institute of Materials Technology & Engineering, Chinese Academy of Sciences, Ningbo, Zhejiang 315201, China
[7]School of Materials Science & Engineering, Taiyuan University of Science and Technology, Taiyuan 030024, China

[a)]Authors to whom correspondence should be addressed: yschen@iphy.ac.cn and jrsun@iphy.ac.cn

ABSTRACT

Due to the strong interlayer coupling between multiple degrees of freedom, oxide heterostructures usually produce distinct interfacial phases with unexpected functionalities. Here, we report on the realization of quasi-two-dimensional ferromagnetic state in ultrathin La$_{0.7}$Sr$_{0.3}$MnO$_3$ (LSMO) layer down to two unit cells (u.c.), being sandwiched by the planar infinite-layer structured SrCuO$_2$ layers (P-SCO). We find the LSMO/P-SCO interface coupling has greatly suppressed the magnetic dead layer of LSMO, resulting in an emergent interfacial ferromagnetic phase. Thus, robust ferromagnetic order can be maintained in the 2 u.c.-thick LSMO layer ($\sim$7.7 Å), showing a Curie temperature of $\sim$260 K and remarkable perpendicular magnetic anisotropy. X-ray absorption spectra reveal notable charge transfer from Mn to Cu at the interface, and thus, resulted preferential d$_{3z^2-r^2}$ orbital occupation for interfacial Mn ions plays an important role in the inducing of perpendicular magnetic anisotropy in quasi-two-dimensional LSMO layer. Our work demonstrates a unique approach for tuning the properties of oxides via an interface engineering of oxygen coordination in perovskite/infinite-layer heterostructures.

Published under an exclusive license by AIP Publishing. https://doi.org/10.1063/5.0183258

I. INTRODUCTION

As a model system with strongly correlated electrons, perovskite transition-metal oxides (TMOs) have attracted great interest due to their abundant properties, such as high-T_C superconductivity, colossal magnetoresistance, ferroelectricity, and multiferroicity.[1–6] In particular, the properties of perovskite oxides can be feasibly tailored via interfacial engineering in artificial heterostructures or superlattices (SLs), generating interfacial phases with distinct functionalities.[7–13] Due to the half-metallicity (nearly 100% spin polarization) and high Curie temperature ($T_c = 370$ K), La$_{0.7}$Sr$_{0.3}$MnO$_3$ (LSMO) is considered as the most promising material for oxide spintronic applications.[14] Along

with the high demand for miniaturization of future spintronic device, a challenge is retaining the ferromagnetism (FM) of oxide film to the two-dimensional (2D) limitation. However, it is widely reported that the magnetic properties, such as spin polarization, saturation magnetization (M_s), and Curie temperature, decline dramatically in ultrathin LSMO films.[15–17] This finally leads to the disappearance of magnetic characters when the film thickness reduces down to a critical value ranging from $\sim$8 to $\sim$30 unit cells (u.c.),[18–20] depending on growth orientation, lattice strain, and chemical conditions. Although it is still under hot debate, several models have been proposed to explain the origin of the magnetic dead layer, such as the orbital reconstruction

caused by symmetry break at the interface/surface,[18,19] the oxygen-nonstoichiometry-induced electron localization, the valence shift due to chemical segregation,[21–23] and the competition between inhomogeneous magnetic phases.[24,25]

Magnetic dead layer has greatly hindered the practical application of LSMO-based devices, and tremendous effort has been made to circumvent it in ultrathin LSMO films.[16–26] Previous works found that the interface/surface orbital reconstruction would promote the $d_{3z^2-r^2}$ occupancy of Mn e_g orbital in the LSMO layer close to substrate, which strongly worsens the double-exchange interactions and favors a C-type antiferromagnetic (AFM) order.[18,19,23] It would be the origin for the thick dead layer in compressively strained LSMO films (on LaAlO₃, LAO) substrate, and also for the thin dead layers in tensely strained (on SrTiO₃, STO) or unstrained (on NdGaO₃, NGO) LSMO films. Inspired by this understanding, a viable route for suppressing magnetic dead layer is to prevent preferential orbital occupation, via diminishing lattice strain and surface effects. Several groups have achieved this idea and made progress in diminishing magnetic dead layer. For example, T_c of a 8 u.c. LSMO film on STO has been greatly enhanced from 100 to 275 K via the introduction of the $[(LaMnO_3)(SrMnO_3)]_2$ buffer layer.[19] By inserting a Sr₃Al₂O₆ buffer layer between LSMO and LAO substrate, the thickness of magnetic dead layer has largely decreased from 8 to 4 u.c.[20] By simultaneously inserting a STO buffer layer and a STO capping layer, Liao *et al.* gained the smallest thickness of magnetic dead layer (~3 u.c.) in LSMO films on the NGO substrate.[26] Though these works are worthwhile, a drawback is that the induced FM state in these ultrathin LSMO films usually exhibits weak magnetic anisotropy (MA), since the MA is closely associated with the preferential orbital occupation according to the Bruno model.[27,28] However, for magnetoelectric devices, a strong MA, especially the perpendicular magnetic anisotropy (PMA), is highly desired for the fast-switching and low-power-consumption applications. Realizing FM order in the ultrathin LSMO layers with considerable high T_c and strong PMA, remains challenging so far.

Benefitting from the strong interlayer coupling between lattice, charge, spin, and orbital degrees of freedom, combining LSMO with a second oxide to form heterostructures or SLs offers an opportunity to resolve this problem.[15–17] The charge transfer and electrostatic boundary conditions at the interface may produce an additional modification to the band structure of LSMO, resulting in charge, orbital, and spin reconstructions. Here, the infinite-layer copper oxide SrCuO₂ (SCO) has come into our sight. Bulk SCO is an AFM insulating oxide, possessing of a layered structure that can be regarded as a perovskite-like framework with missing apical oxygen.[29,30] Thick SCO films usually favor a planar (P)-type oxygen-coordination, i.e., the positively charged Sr²⁺ and negatively charged CuO₂²⁻ planes are alternately stacked along the direction normal to film plane. Upon reducing thickness, the P-type structure of SCO film transforms to a chain (C)-type structure with CuO₂²⁻ planes perpendicular to the film plane, avoiding the electrostatic polar instability.[31–33] Thus, when grouping SCO with LSMO, the mismatch of apical oxygen and the large polarity discontinuity will bring an additional coupling effect at the interface, which may lead to unusual properties that cannot be obtained in bare films or ordinary perovskite/perovskite heterostructures.[16–26]

In this paper, high-quality LSMO/SCO SLs were epitaxially grown on the TiO₂-terminated SrTiO₃ (STO) substrates. Emergent interfacial FM state with remarkable PMA was successfully induced in the ultrathin LSMO layers (down to 2 u.c., ~7.7 Å) when sandwiched in the 10-u.c.-thick P-SCO layers. The Curie temperature of such interfacial FM phase is as high as ~260 K for the LSMO layer of 2 u.c. and quickly increases to 300 K when the LSMO layer thickness is larger than 4 u.c. This is in sharp contrast with the LSMO bare films with a magnetic dead layer of at least 8 u.c. (~3 nm). The x-ray linear dichroism (XLD) measurements clearly reveal the preferential $d_{3z^2-r^2}$ occupancy of Mn e_g orbital at the LSMO/P-SCO interface, which is responsible for the notable PMA of interfacial LSMO layer. The simultaneous realization of robust FM order and PMA in the quasi-2D LSMO layer at room temperature is of paramount importance for the potential applications in all-oxide spintronic devices, such as spin–orbit torque device, magnetic tunnel junction device, and low-power-consumption memory device.[34–37] Our work demonstrates that the perovskite/infinite-layer interface coupling can provide an effective means to manipulate the orbital configuration and associated physical properties of oxides, paving pathways toward the advancement of oxide electronics.

II. RESULTS AND DISCUSSION
A. Structural analysis

[LSMOₘ/SCOₙ]₁₀ (L_m/S_n) superlattices, with 10 repetitions of m (n) unit cells of LSMO (SCO) in each period, are epitaxially grown on TiO₂ single-terminated (001)-STO substrates by the technique of pulsed laser deposition. As mentioned above, the SCO layer will present a P-type or C-type structure depending on its thickness. To compare the coupling effect at the LSMO/P-SCO and the LSMO/C-SCO interfaces, two series of L_m/S_n SLs, with SCO layer thicknesses of 2 and 10 u.c., respectively, and LSMO layer thickness ranging from 2 to 30 u.c. were prepared. The schematic diagrams for these two kinds of heterostructures are shown in Fig. 1(a), and the corresponding x-ray diffraction (XRD) spectra around the (002) peak of STO substrate are shown in Fig. 1(b) and Fig. S1 of the supplementary material. The XRD data of a LSMO bare film (50 nm) and a SCO bare film (16 nm) are also presented as references. As shown, clear satellite peaks corresponding to the SL structure and the finite-size oscillations arising from the thickness fringes are identified for all samples, revealing the high quality of the SLs. To determine the in-plane strain state of the SLs, the reciprocal space mapping (RSM) of the (103) reflection is measured. Taking $[L_{30}/S_{10}]_{10}$ as an example, the diffraction spots of the SL [marked by red arrow in Fig. 1(c)] locate just above that of the STO, i.e., the SL is coherently strained to the substrate without lattice relaxation. This conclusion is also applicable to other samples.

As reported, the critical thickness for the C–SCO films deposited on STO is about 3–5 u.c., above which P-SCO prevails.[31–33] It can be clearly identified from out-of-plane lattice constants: $c = \sim3.464$ Å ($2\theta = 52.8°$) for P-SCO or ~3.8 Å ($2\theta = 47.8°$) for C-SCO. Thus, when grouping LSMO and P-SCO or C-SCO layers into SLs, the (002) main peak (SL₀), which reflects the average c-axis lattice constants of SLs, would show quite different features. In Fig. 1(d), we summarize the c-axis lattice constants of the two series of SLs obtained from the θ–2θ scans. Generally, the c-axis lattice constants of the L_m/S_n SL can be calculated using the formula as $c_{SL} = (n * c_{SCO} + m * c_{LSMO})/(n + m)$, where c_{SCO} and c_{LSMO} are lattice constants of the SCO layers and LSMO layers, respectively. As shown in Fig. 1(d), there is a good agreement between the measured data and the fitting curves. Moreover, the c-axis lattice constant of the SCO layers in the SL
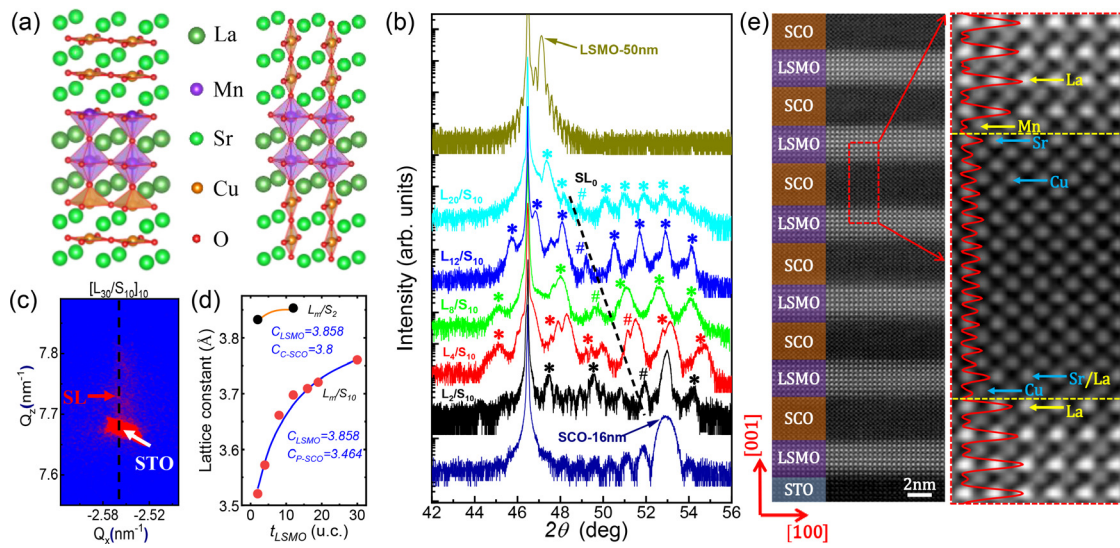
FIG. 1. (a) Schematic views of the P-SCO/LSMO (left panel) and C-SCO/LSMO (right panel) heterostructures. (b) XRD patterns for the $[LSMO_m/SCO_{10}]_{10}$ SLs (noted as L_m/S_{10}) on STO. # indicates (002) main peak (SL_0) and ∗ indicate satellite peaks. (c) RSM around (103) reflection for L_{30}/S_{10} SL on STO. (d) The deduced out-of-plane lattice constants as functions of the thickness of LSMO layer (t_{LSMO}). The red points are the results of the L_m/S_{10} SLs with m ranging from 2 to 30, and the black points are the results of the L_m/S_2 SLs with m = 2 and 12. (e) High-angle annular dark-field (HAADF) image of the cross section of the L_8/S_{10} SLs, recorded along the [100] zone axis. The LSMO and SCO sublayers are marked by purple and orange colors, respectively. The right panel is an enlarged view of the lattice image.

structure is directly deduced from the above formula. It is ∼3.80 Å for the SCO layers in L_m/S_2 SLs and ∼3.46 Å for the SCO layers in L_m/S_{10} SLs, well consistent with the reported results for C-SCO and P-SCO. All these results confirm the formation of the LSMO/SCO SLs with well-ordered target structures.

To get the information about atomic-scale structure, the lattice image of L_8/S_{10} SL is collected by high-resolution scanning transmission electron microscope (STEM). Figure 1(e) presents the high-angle annular dark-field (HAADF) image of the cross section of L_8/S_{10}, recorded along the [100] zone axis. Due to the strong brightness contrast between La and Sr atoms, the alternate stacking of LSMO and SCO layers can be clearly seen, confirming the coherent and epitaxial growth of the periodic structure with atomically flat interfaces. The line profile analysis of the atomic contrast along the vertical direction is further shown in the right panel. We can see that the upper LSMO/SCO interface is very sharp, without interlayer mixing. In contrast, partial Sr^{2+} ions in the first Sr–O layer at the bottom SCO/LSMO interface are replaced by La^{3+} ions, resulting in an A-site intermixing within one unit cell. Fortunately, this will not affect the analysis of FM phases since $La_xSr_{1−x}CuO_2$ also exhibits the AFM order as SCO does.[38]

B. Magnetic characterization

As mentioned above, a strong coupling effect is expected at the perovskite/infinite-layer interface due to the mismatch of apical oxygen and strong polarity discontinuity. Thus, we are interested in what will happen when the LSMO layer is in close proximity to the SCO layer of different structures. The most remarkable observation is the great suppression of magnetic dead layer in the LSMO/P-SCO heterostructure, i.e., the L_m/S_{10} SLs. Figures 2(a)–2(e) and Fig. S2 show the temperature-dependent magnetization curves (M–T) of the L_m/S_{10} SLs

with m ranging from 2 to 30 u.c., measured by applying an in-plane or out-of-plane magnetic field of 20 Oe. The M–T curves measured in higher magnetic fields are given in Fig. S3 of the Supplementary material. A rapid increase in magnetization is displayed at ∼260 K in the out-of-plane M–T curve of the L_2/S_{10} SL, followed by a tendency toward magnetic saturation with further cooling. This feature signifies the retaining of FM order in 2-u.c.-thick LSMO layers when sandwiched by the P-SCO layers. M–T curves are also obtained for the $[L_2/S_{10}]_N$ SLs with different repetitions (Fig. S4 of the Supplementary material). The magnitude of the magnetic moment shows a dependence on repetition N, whereas the Curie temperature is essentially independent of N. Considering the ultrathin LSMO FM layers are separated by the AFM P-SCO layers with much larger thickness, they can be regarded as a series of quasi-2D FM layers. T_{C-s} is ∼260 K for the L_2/S_{10} SL and ∼300 K for the L_4/S_{10} SL. By contrast, the LSMO bare films show no FM order in the case of 2 or 4 u.c., and a T_C of ∼300 K can be only obtained in the bare film with a thickness above 15 u.c.[15,18–26] In addition, when further increasing the thickness of the LSMO layer, a second magnetic phase with relatively low transition temperature T_{C-i} appears. As demonstrated by the in-plane M–T curves in Figs. 2(c)–2(e), two inflexion points that correspond to different T_C of the two FM phases are clearly seen in L_m/S_{10} SLs for m ≥ 8. The dependence of T_{C-s} and T_{C-i} on LSMO thickness m is summarized in Fig. 2(k). We can see that T_{C-s} rapidly reaches a saturation value of ∼320 K, while T_{C-i} is relied upon LSMO thickness more greatly, increasing from ∼200 K for the L_8/S_{10} SL to ∼265 K for the L_{30}/S_{10} SL. A reasonable assumption is that the first FM phase with a relatively constant T_{C-s} is an interfacial phase, originating from the LSMO/P-SCO interface coupling. This interfacial phase has no dead layer due to interfacial reconstruction. In contrast, the second FM phase that begins to occur in the SL with thick LSMO layers may be the inner phase,
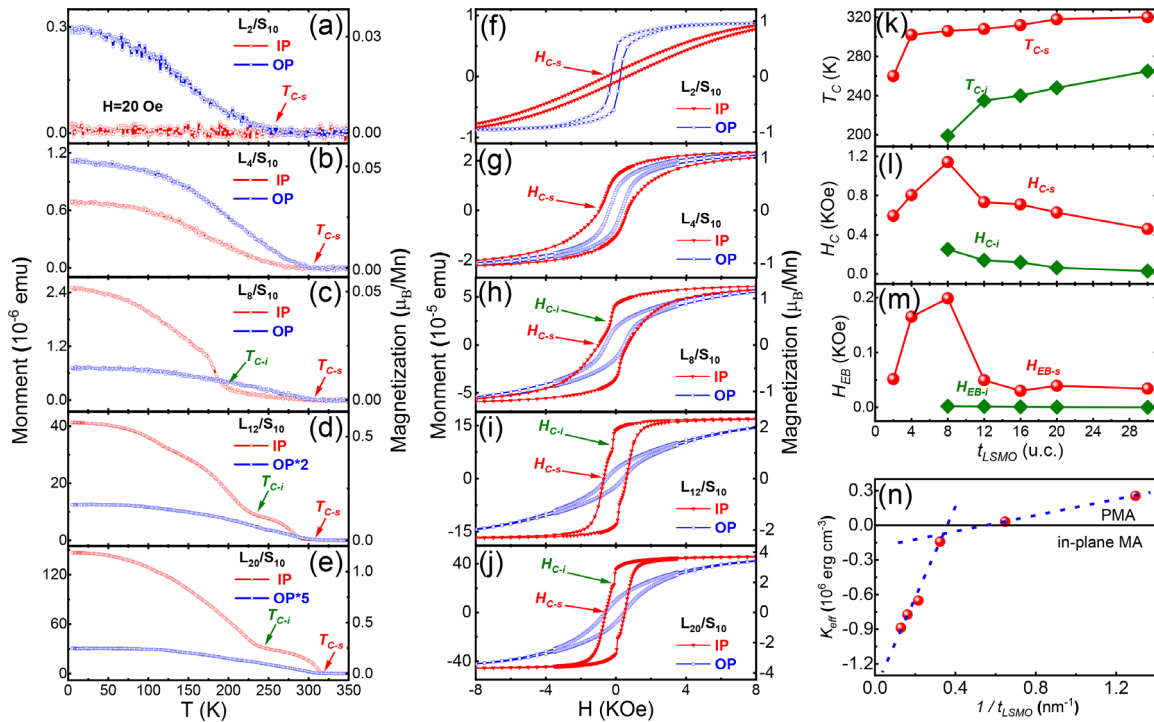
FIG. 2. (a)–(e) M–T curves of L_m/S_{10} SLs. A magnetic field of 20 Oe is applied along the in-plane direction (red lines) or the out-of-plane direction (blue lines). (f)–(j) In-plane and out-of-plane magnetic hysteresis loops of L_m/S_{10} SLs, measured at 5 K after the $+3$ T field-cooling from room temperature. Summary of (k) the curie temperature (T_c), (l) the coercive field (H_c), and (m) the exchange bias (H_{EB}) for the L_m/S_{10} SLs. (n) Calculated K_{eff} of each sample as a function of $1/t$ (t is the LSMO thickness).

forming in the intermediate region of the LSMO layers. It exhibits a significantly thickness-dependent $T_{C\text{-}i}$, similar to the LSMO bare films.

Another important information delivered by the M–T curves is the change in MA with the increase in the layer thickness of LSMO. From the first glance, the out-of-plane M–T curves are above the in-plane M–T curves for the L_2/S_{10} and L_4/S_{10} SLs, suggesting the occurrence of PMA. Accompanying the appearance of LSMO inner phase, the sequence of the out-of-plane and in-plane M–T curves reverses, implying a transition from PMA to the in-plane MA. To further determine the anisotropy constant, we measured the magnetic-field-dependent magnetization curves (M–H) for the L_m/S_{10} SLs [shown in Figs. 2(f)–2(j) and Fig. S2 of the Supplementary material], measured with a cooling field of $+3$ T at 5 K. A positive anisotropy constant (magnetic easy axis along the out-of-plane direction) of $K_{eff} = +3 \times 10^5$ erg/cm^3 is obtained for the L_2/S_{10} SL. It continuously declines with the increase in LSMO thickness and finally comes to a negative value of $K_{eff} = -9 \times 10^5$ erg/cm^3 for the L_{20}/S_{10} SL. Moreover, when two phases coexist in the LSMO layer with thickness equal or greater than 8 u.c., the shape of the hysteresis loops changes, showing evidence of two separate coercive fields (H_c). As shown in Fig. S5 of the Supplementary material, we can disassemble the in-plane M-H curve into two subcurves, and thus, H_c and the exchange bias field H_{EB} of each phase can be determined individually. Here, $H_c = |H_+ - H_-|/2$ and $H_{EB} = |H_+ + H_-|/2$, where H_+ and H_- denote the right and left data of coercivity as the magnetization reaches zero, respectively. Figures 2(l) and 2(m) plot H_c and H_{EB} of the two FM phases as a function of LSMO thickness, respectively. $H_{c\text{-}s}$ of the interfacial phase

undergoes first an increase and then a decrease with LSMO thickness, while the inner phase presents a much smaller coercivity $H_{c\text{-}i}$ that monotonically decreases with LSMO thickness. Furthermore, the exchange bias effect, with a substantial shift of H_{EB} after the $+3$ T field cooling, is only observed for the interfacial phase. This is understandable since the LSMO interfacial phase is in close proximity to the AFM SCO layers, while the inner LSMO phase does not.

The above-mentioned magnetic measurements strongly suggest the appearance of interfacial phase in the LSMO/P-SCO heterostructure. It overcomes the dead layer effect and retains the FM order in the LSMO layer of 2 u.c. in thickness. Meanwhile, the interfacial phase exhibits a high T_c and a fairly strong PMA, and both features are desired by practical applications. Obviously, the influence of the LSMO/P-SCO interface coupling on the neighboring LSMO layer has limited thickness. When LSMO thickness exceeds a critical value, the inner phase begins to occur. It shows similar features as those observed in LSMO bare films on STO, i.e., strongly thickness-dependent $T_{c\text{-}i}$, small $H_{c\text{-}i}$, and in-plane MA. For comparison, the M–T and M-H curves for a SCO single film (40 u.c. in thickness) and LSMO single films with thickness ranging from 2 to 12 u.c. are also given in Fig. S6 of the supplementary material. Comparing with LSMO single films, the magnetization and Tc of LSMO ultrathin layers sandwiched between P-SCO layers are enhanced significantly, proving the effect of interface coupling. To get an idea about the correlation length of interface coupling, a phenomenological model is proposed based on the dependence of K_{eff} on LSMO thickness. We consider that the effective anisotropy constant K_{eff} can be separated into three contributions: the

volume anisotropy energy for the interfacial phase K_{v1} (erg cm^{-3}) and the bulk phase K_{v2} (erg cm^{-3}), and the volume-independent contribution K_s (erg cm^{-2}) originated from LSMO/P-SCO interface coupling. If the interfacial phase has a thickness of t_c, K_{eff} will show a step dependence on the thickness of LSMO (t), approximately described by the following two formulas:[39–41]

$$K_{eff} = K_{v1} + K_s/t, \quad t \le t_c,$$
$$K_{eff} = K_{v1}t_c/t + K_{v2}(t - t_c)t + K_s/t, \quad t > t_c. \quad (1)$$

The term K_s/t represents the decay of the interface contribution in the inner region of the LSMO layer. As plotted in Fig. 2(n), the $K_{eff} - 1/t$ relationship obtained from experimental measurement can be well fitted by the above-mentioned formulas, showing two line segments. A quantitatively analysis of the slopes and intercepts of the two line segments gives a t_c of 7–8 u.c. It means that the interfacial phase is localized within 4 u.c. LSMO layer near the interface. A positive value of 0.044 erg cm^{-2} for K_s is also deduced, proving that it is the LSMO/P-SCO interface coupling that causes the PMA.

We would like to emphasize that the FM interface phase only appears at the LSMO/P-type SCO interface. When the P-type SCO layer changes to C-type SCO layer with the decrease in layer thickness, the FM interfacial phase disappears. For example, as shown in Figs. S7(a) and S7(c) of the supplementary material, the interfacial phase is not found in the L$_{12}$/S$_2$ SL and only one transition at ~240 K is observed, which just corresponds to the inner phase in the L$_{12}$/S$_{10}$ SL. This is to say, the interfacial FM phase does not exist in the LSMO/C-SCO heterostructure. Naturally, when reducing the LSMO thickness to 2 u.c., the L$_2$/S$_2$ SL shows no FM signal at all [Figs. S7(b) and S7(d)], implying the occurrence of magnetic dead layer.

C. PNR and x-ray spectroscopic measurements

The magnetic measurements reveal the different T_c and H_c of interfacial and inner FM phases in LSMO layers when interfacing with

P-SCO. To get an idea about the spatial distribution of the two FM phases, we performed measurements of polarized neutron reflectometry (PNR), which can reconstruct the magnetic depth profile across the interface. Figure 3(a) shows the neutron reflectivity of L$_{16}$/S$_{13}$ SL as a function of wave vector transfer $q = 4\pi\sin\theta/\lambda$, obtained at 120 K with the neutron spin parallel (R^{++}) or antiparallel (R^{--}) to the applied magnetic field (1.2 T), where θ is the incident angle of the neutron beam and λ is the neutron wavelength. The inset plot in Fig. 3(a) is the spin-asymmetry defined by SA = $(R^{++} - R^{-})/(R^{++} + R^{-})$, which provides the information about the depth variation of the net magnetization across the interface. Here, to make the Bragg peaks appear within the sensitive region of PNR,[42] the L$_{16}$S$_{13}$ SL with relatively thicker SL period is chosen, which demonstrates similar interfacial and inner FM phases as those observed in the L$_{16}$S$_{10}$ SL (see Fig. S2). Four different models were considered for the PNR fitting, and the details are given in Fig. S8 of the Supplementary material. By comparison, the best curve fitting for the PNR and SA data [solid lines in Fig. 3(a)] is obtained based on the model shown in Fig. 3(b). It outputs the spatially resolved nuclear scattering length density (nSLD) and magnetic scattering length density (mSLD) of the SL sample. Indeed, the interfacial LSMO phase with a magnetic moment of ~2.9 μ_B/Mn and the inner LSMO with a lower magnetic moment of ~1.9 μ_B/Mn are clearly identified in the mSLD curve at 120 K. The thickness of the interfacial LSMO phase of ~4 u.c. also well agrees with that deduced from macroscopic magnetic measurements. Significant reduction of magnetization occurs at the first and the 10th LSMO layers is possible due to the different boundary conditions at the substrate interface and sample surface.[43–45]

Next, to get more information on the emergent FM phase at the LSMO/P-SCO interface, we perform the soft x-ray absorption (XAS) spectra measurements around Mn L-edge for the samples of L$_4$/S$_{10}$, L$_{12}$/S$_{10}$, L$_{12}$/S$_2$ SLs, and a LSMO bare film. We first focus on the changes in valence states of Mn ions, revealed by the XAS results with the 90° incident angle in Fig. 3(c). As shown, the peak position of
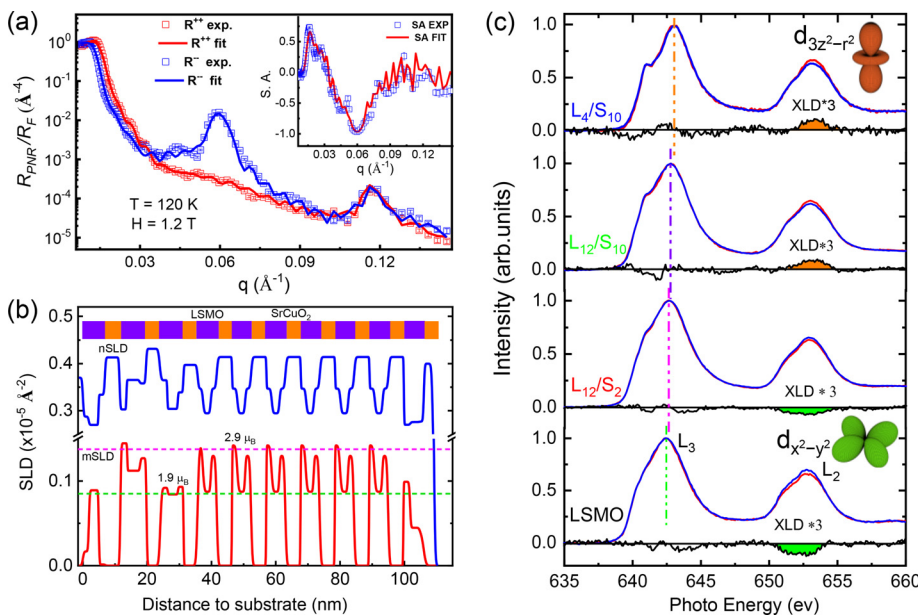
FIG. 3. (a) Reflectivity curves for spin-up (R^{++}) and spin-down (R^{--}) polarized neutrons as a function of wave vector q ($= 4\pi \sin\theta_i/\lambda$) measured for the L$_{16}$/S$_{13}$ SL, where θ_i is the incident angle and λ is the neutron wavelength. PNR measurements were performed at 120 K after field-cooling under 1.2 T. (b) The best-fit models of the structural and magnetic depth profiles for the L$_{16}$/S$_{13}$ SL. (c) Normalized x-ray absorption spectroscopy (XAS) of Mn $L_{2,3}$ edge for the L$_4$/S$_{10}$, L$_{12}$/S$_{10}$, L$_{12}$/S$_2$, and LSMO bare film on STO. The blue (or red) line with the intensity of I_c (or I_{ab}) is obtained by the oblique (or normal) incidence of the polarized x-ray beam. The deduced XLD spectrum of ($I_{ab} - I_c$) is given by the black line below. The vertical dashed lines indicate the peak position of the L$_4$/S$_{10}$ (yellow), L$_{12}$/S$_{10}$ (violet), L$_{12}$/S$_2$ (purple) SLs, and LSMO bare film (green).

Mn-L_3 displays a significant right shift in the L_4S_{10} (643.0 eV) or $L_{12}S_{10}$ (642.8 eV) SL, compared with that of the LSMO bare film (642.4 eV). This indicates an increase in the valence state of Mn ions when the LSMO/P-SCO interface is formed. For the Mn ions, the 0.6 eV peak shift between the L_4S_{10} SL and the LSMO bare film is comparable to or greater than that for a LSMO film with a MgO or NdGaO$_3$ capping layer reported by Valencia *et al.*, which was considered to be an indication of an increase in the Mn^{4+} content by about 15%–18% at the interface.[46] Such a variation in the valence state implies the charge transfer between B-site ions at the interface, i.e., electrons transfer from Mn^{3+} ions to Cu^{3+} (or Cu^{2+}) ions in our samples. As shown in Fig. 1(a), the mismatch of apical oxygen between LSMO and P-SCO will lead to two types of interfaces: [CuO$_2$]-[(La,Sr)] -[MnO$_2$] and [CuO$_2$]-[(La,Sr)O]-[MnO$_2$]. The charge transfer at the former type interface could be negligibly small due to the missing of apical oxygen. Thus, considering the obvious increase in the Mn valence state, the [CuO$_2$]-[(La,Sr)O]-[MnO$_2$] connection should be more preferred at the LSMO/P-SCO interface. This may be ascribed to a relatively high oxygen pressure adopted for the deposition of the SCO layer. In this situation, the Cu site may be mainly caged by an oxygen pyramidal geometry at the interface, forming the CuO$_5$-pyramid/ MnO$_6$-octahedron connections and resulting in the strong charge transfer. The high energy shift of the Mn-L_3 peak is also observed for the L_{12}/S_2 SL (642.6 eV) with the LSMO/C-SCO interface, though it is smaller compared with that observed in the L_{12}/S_{10} or L_4/S_{10} SL. This is possibly because of the different Fermi level between P-SCO and C-SCO. Compared with the Cu^{2+} valence state in C-type SCO, the CuO$_5$ pyramids at LSMO/P-SCO interface would result in an electron lost at central Cu sites, causing a relatively higher valence state of Cu$^{2+\delta}$ with a lower Fermi energy. Therefore, the CuO$_5$-pyramid/MnO$_6$-octahedron connections would result in much stronger Mn-to-Cu charge transfer at the LSMO/P-SCO interface than that of the CuO$_4$-chain/MnO$_6$-octahedron connections at the LSMO/C-SCO interface. It may be the reason for the occurrence of distinct interfacial FM phase. The XAS data around Cu L-edge for the SL samples and the bare SCO film are provided in Fig. S9 of the supplementary material. The lower energy shifts of ~0.2 eV for the L_4/S_{10} SL and ~0.4 eV L_{12}/S_2 SL are observed as compared to the bare SCO film. It should be noticed that the charge transfer cannot affect the whole 10 u.c.-thick SCO layers in the L_4/S_{10} SL. Thus, the amplitude of the energy shift of Cu L-edge is lower that is estimated in the L_4/S_{10} SL making it even lower than that obtained in the L_{12}/S_2 SL. More precise estimation of the Cu valence shift is obtained by the layer-resolved EELS as will be shown later.

In addition to the changes in the valence state, the strong charge transfer may also cause an orbital reconstruction. Generally, the Mn to Cu charge transfer is intermediated by the apical O $2p_z$ orbital. It causes an overlap of the $d_{3z^2-r^2}$ orbitals for interfacial Mn and Cu ions, forming a Mn-O-Cu covalent bond. This will alter the energy band relation near the Fermi surface, leading to orbital reconstruction. Figure 3(c) compares the XLD spectra of Mn L-edge measured for the L_4/S_{10}, L_{12}/S_{10}, L_{12}/S_2 SLs, and LSMO bare film. The details for the XLD measurement are given in Sec. IV. As reported,[47–49] the XLD signal around the high energy L_2 absorption peak (650–655 eV) is very sensitive to the occupancy situation of the e_g orbitals: larger absorption for one polarization indicates more empty states in the e_g band and thus a lower occupancy. Since the $d_{3z^2-r^2}$ orbital is in the OP direction, while the $d_{x^2-y^2}$ orbital lies in the film plane, the spectral intensities I_c

and I_{ab} should mainly be proportional to the hole content in the $d_{3z^2-r^2}$ and $d_{x^2-y^2}$ orbitals, respectively. We can see that the XLD signals of the L_4/S_{10} and L_{12}/S_{10} samples show an obvious positive peak. It indicates that the preferentially occupied orbital is $d_{3z^2-r^2}$ at LSMO/ P-SCO interface. This is reasonable since the charge transfer at the LSMO/P-SCO interface is intermediated by the apical O $2p_z$ orbitals, which forms the Mn–O–Cu covalent bond consisting of $d_{3z^2-r^2}$ orbitals of Mn/Cu ions. This lowers the Mn $d_{3z^2-r^2}$ orbital and makes it to be preferentially occupied. Moreover, though charge transfer also occurs at the LSMO/C-SCO interface, it is not strong enough to cause orbital reconstruction. The negative XLD signal indicates that the preferentially occupied orbital is still $d_{x^2-y^2}$ in the L_{12}/S_2 SL, similar to the LSMO bare film under tensile strain. According to the Bruno model, the spins of the Mn ions prefer to follow the direction of the orbital momentum.[27,28] Thus, it is the preferential electron occupancy of Mn $d_{3z^2-r^2}$ orbital that causes the abnormal PMA in the interfacial phase of LSMO/P-SCO SLs. With the increase in the LSMO thickness, the contribution from the inner LSMO phase that exhibits a preferential occupancy of $d_{x^2-y^2}$ orbital increases, and finally, the effective MA turns to the in-plane direction. The x-ray spectroscopy investigation clearly proves the retaining of preferential $d_{3z^2-r^2}$ orbital occupation in the quasi-2D FM phase at the LSMO/P-SCO interface. This observation is opposite to the previous thought of removing magnetic dead layer by suppressing the orbital polarization, suggesting the specificity of perovskite/infinite-layer interface coupling.

Notably, for the SLs with thicker LSMO or P-SCO layers, charge transfer may mainly take place in the interface regions, resulting in interfacial phases with distinct properties. A further issue to be addressed is the thickness of each interfacial layer. Figure 4(a) is the HAADF image of a local area of the SL and the annular bright-field (ABF) images acquired simultaneously to determine the O anions. The ABF lattice images of the upper LSMO/SCO interface and the bottom SCO/LSMO interface are magnified in Figs. 4(b) and 4(c), respectively. Here, the small dark dot between the large cation dots represents oxygen anions, which will fade out when oxygen anions are replaced by oxygen vacancies. As expected, the LSMO layer has a perovskite structure with MnO$_6$ octahedral, while the SCO layer has an infinite-layered structure with O anions existing only in the Cu–O planes but being absent in the Sr planes. An important thing is that the O anions can be observed at most of the oxygen sites in the interfacial La/Sr–O layer. This suggests a CuO$_5$-pyramid/MnO$_6$-octahedron connection at the interface (see Fig. S10 of the supplementary material). To determine the range of charge transfer, spatially resolved EELS spectra around the Mn-L_3 and Cu-L_3 edges were further investigated for the L_8/S_{10} SL, measured along the [001] direction of the green box region as shown in Fig. 4(a). As shown in Fig. 4(d), the Mn-L_3 edge exhibits a high-energy shift within two to three Mn–O layers near the upper (or bottom) interface. Correspondingly, the Cu-L_3 edge shifts to low energies for the first two Cu–O layers near the interface.

D. Magneto-transport characterization

Next, we turn our attention to the magneto-transport properties of the LSMO/P-SCO SLs. Figure 5(b) gives the angle-dependent magnetoresistance for two typical SLs (L_4/S_{10} and L_{12}/S_{10}) at 5 K. As shown in Fig. 5(a), the electric current is applied along the [100] direction and the magnetic field of 3 T is rotated in the (100) plane that is perpendicular to the current. The anisotropic magnetoresistance is calculated by
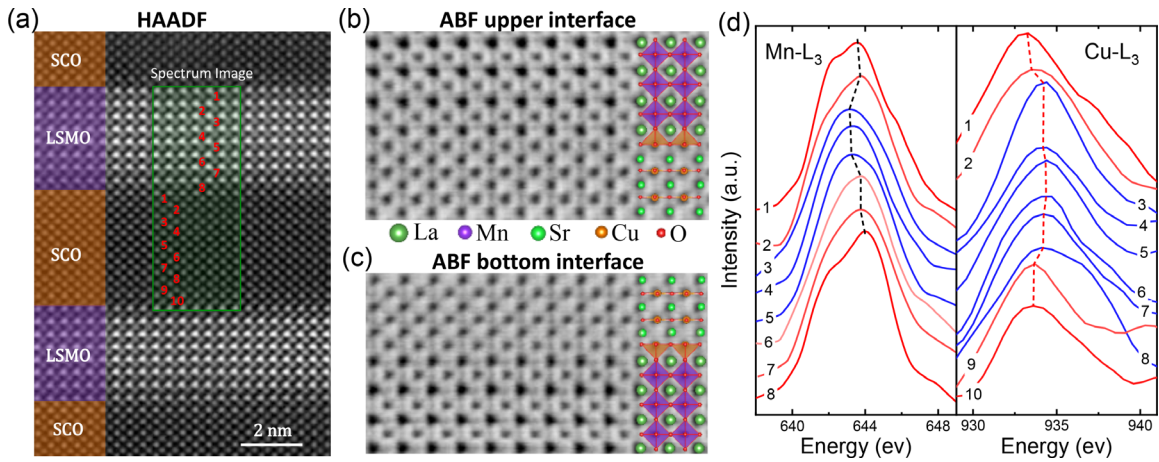
FIG. 4. (a) STEM-HAADF image on the local region of the L_8/S_{10} SLs. The green rectangular box indicates the region where the EELS spectra were acquired. The corresponding ABF images for the (b) upper LSMO/SCO and (c) bottom SCO/LSMO interfaces are also measured. Schematic diagrams show the CuO_5-pyramid/MnO_6-octahedron connections at the interface. (d) Layer-resolved EELS spectra of the Mn L_3 edge and Cu L_3 edge.

$AMR = (R_\theta - R_{90})/R_{90} \times 100\%$, where R_θ is the resistance measured with the magnetic field forming an angle of θ with the [010] direction. Though both AMRs of the two SLs show twofold symmetry, the peak/valley positions reverse. As shown, the minimal resistance of the L_4/S_{10} SL occurs in the out-of-plane [001] direction, while it occurs in the in-plane [010] direction for the L_{12}/S_{10} SL. For magnetic materials, the minimal spin-flip scattering will occur in the direction of magnetic easy axis since dominant spin is parallelly aligned with the magnetic field.[50,51] This usually causes the minima value in the AMR-θ curves. Thus, the AMR result of the L_4/S_{10} SL again supports the PMA of the interfacial phase of LSMO/P-SCO SL. With increased LSMO layer thickness, the inner phase begins to occur and the MA turns to the in-plane direction.

Moreover, the magnetic decoupling between interfacial phase and inner phase has also been reflected in the transport measurements. Figures 5(c) and 5(d) depict the magnetic field dependence of
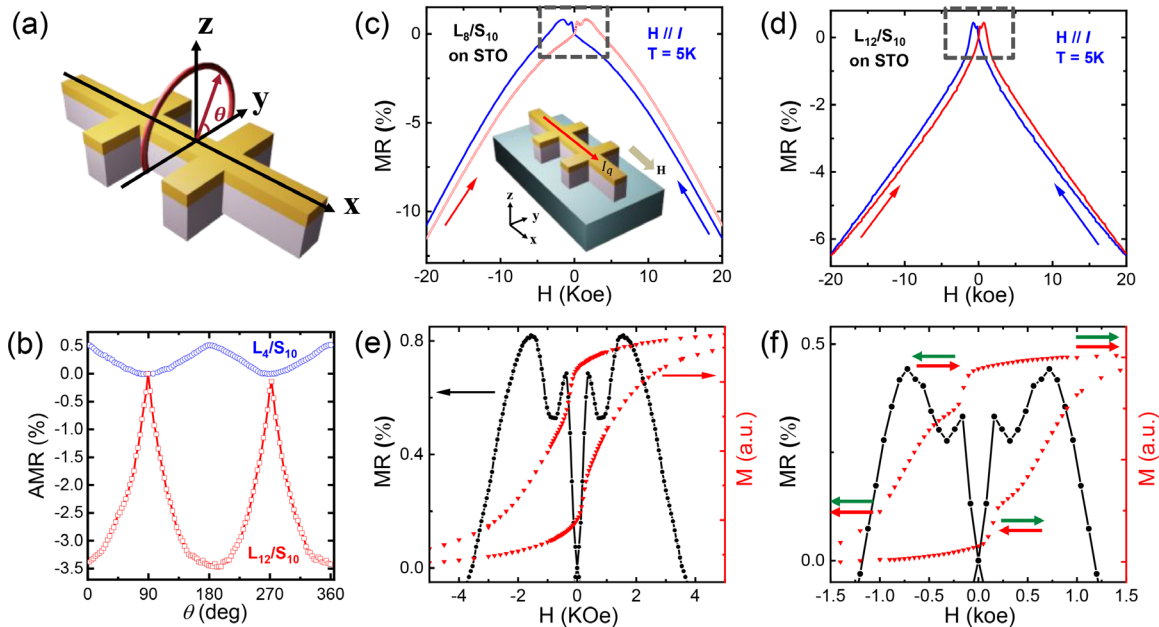
FIG. 5. (a) The geometry for the AMR measurements. (b) AMR for L_4/S_{10} and L_{12}/S_{10} SLs at 5 K, measured with a magnetic field of 3 T rotated in the yz plane. MR-H curves for (c) the L_8/S_{10} and (d) L_{12}/S_{10} SLs, obtained at 5 K. The magnetic field and electric current are both applied along the in-plane [100] direction. (e) and (f) The enlarged low field regions of the MR–H and M–H curves for the L_8/S_{10} and L_{12}/S_{10} SLs, respectively. The parallel and antiparallel resistance states between the interfacial phase and bulk phase are marked by arrows.

$MR = (R_H - R_0)/R_0$ for the L_8/S_{10} and L_{12}/S_{10} SLs at 5 K, where R_0 and R_H are the longitudinal resistances measured without and with a magnetic field parallel to electric current, respectively. In addition to the negative MR hysteresis loops as generally observed in LSMO bare films, the MR–H curves of the SLs show two platform-like peaks in the low field region. To clear show these, we enlarge the low field region of the two curves in Figs. 5(e) and 5(f). The M–H curves measured from the same SLs are also given as reference. With magnetic field scanning from one polarity to another, the MR-H curves show two sub-peaks successively, which just correspond to the H_{c-s} of interfacial phase and H_{c-i} of inner phase, respectively. With magnetic field scanning from one polarity to another, the MR–H curves show two sub-peaks successively, which just correspond to the H_{c-s} of interfacial phase and H_{c-i} of inner phase, respectively. For example, when the magnetic field scans from positive to negative values, the magnetization of the interfacial and inner LSMO phases is in parallel at first. When the magnetic field reaches $-H_{c-i}$, the magnetization of the inner LSMO phase reverses, whereas that of the interfacial phase does not. An antiparallel magnetic state between interfacial and inner phases, thus, occurs, until the magnetic field reaches $-H_{c-s}$. These processes result in a platform with a higher resistance between $-H_{c-i}$ and $-H_{c-s}$, similar to the giant magnetoresistance effect that is usually observed in magnetic metal multilayers. The difference is that the FM layers in the SL structure are formed by LSMO only and the distinct parallel/antiparallel resistance states are caused by the magnetic decoupling of the interfacial LSMO layer with the inner LSMO layer. It is just another sign that the P-SCO film has strongly pinned the neighbored LSMO layer, resulting in an interfacial FM phase with fascinating magnetic features such as no magnetic dead layer and PMA.

III. CONCLUSION

In summary, we report a quais-2D FM phase induced by the LSMO/P-SCO interface coupling. It overcomes the magnetic dead layer effect and retains the FM order in ultrathin LSMO layer up to 2 u.c. (~7.7 Å), possessing of a considerably high Tc of ~260 K and notable PMA. As far as we know, this is the first observation of room-temperature PMA for LSMO-based systems. These excellent properties demonstrate the promising application in the design of fast-switching and low-power-consumption oxide magnetoelectric devices. Based on the XAS analysis, we consider the formation of CuO_5/MnO_6 connections along with the stronger Mn-to-Cu charge transfer at the LSMO/P-SCO interface is the origin for the occurrence of such quasi-2D FM phase. Its PMA is just originated from the preferential $d_{3z^2-r^2}$ orbital occupation as revealed by XLD. Our work demonstrates a feasible way to eliminate the magnetic dead layer in LSMO ultrathin films, opening avenues toward advanced oxide electronics.

IV. METHODS
A. Sample fabrication

High quality $(LSMO_m/SCO_n)_{10}$ SLs were epitaxially grown on (001)-oriented STO substrates by the technique of pulsed laser deposition (KrF, $\lambda = 248$ nm). During film growth, the substrate temperature was kept at 600 °C and the oxygen pressure was set to 20 Pa. The adopted fluence of laser pulse was 1.2 J/cm^2, and the repetition rate was 2 Hz. The deposition rate for the LSMO and SCO layers has been carefully calibrated by the technique of small angle x-ray reflectivity (XRR, see Fig. S1 of the supplementary material).

B. Sample characterization

The surface morphology of as-prepared films was measured by atomic force microscopy (AFM, SPI 3800N, Seiko). The crystal structure was determined by a high-resolution x-ray diffractometer (D8 Discover, Bruker) with the Cu-Kα radiation. The magnetic properties were measured by a Quantum Designed vibrating sample magnetometer (VSM-SQUID) in the temperature range of 5–350 K, with the maximal magnetic field of 3 T. The magnetic field was applied along the out-of-plane direction or the in-plane direction of the (001) films. The transport measurements were performed in Quantum Designed physical property measurement system (PPMS) with standard Hall bar geometry.

C. Polarized neutron reflectometry (PNR)

PNR experiments were performed at the MR beamline of the Chinese Spallation Neutron Source (CSNS). The samples were field-cooled and measured at 1.2 T along the in-plane direction. PNR measurements were carried out at 120 K in the specular reflection geometry with wave vector transfer (q) perpendicular to the surface plane. The neutron reflectivity was recorded as a function of q for the spin-up (R^{++}) and spin-down (R^{--}) polarized neutrons. These neutron reflectivities were normalized to the asymptotic value of the Fresnel reflectivity ($R_F = 16\pi^2/q^4$) for a better illustration. The difference between R^{++} and R^{--} was calculated as the spin asymmetry $SA = \frac{(R^{++}-R^{--})}{(R^{++}+R^{--})}$. The PNR data were fitted using the GenX software.

D. X-ray spectroscopic measurements

The x-ray absorption spectroscopy (XAS) measurements are performed at the beamline BL08U1A in the Shanghai Synchrotron Radiation Facility at room temperature in a total electron yield mode. The spectra of Mn L edge are measured by changing the incident angle of linearly polarized x-ray beam. The sample's scattering plane was rotated by 30° and 90° with respect to the incoming photons. E is the electric field of the x-ray. I_{ab} ($E//[100]$ or $[010]$) and I_c ($E//[001]$) are the absorption intensities corresponding to the in-plane and out-of-plane directions, respectively. XLD is calculated by $I_{ab} - I_c$.

SUPPLEMENTARY MATERIAL

See the supplementary material that is available from the AIP Publishing or from the author.

Synchrotron Radiation Facility (SSRF) and Spallation Neutron Source Science Center for the PNR characterizations. This work was supported by the Synergetic Extreme Condition User Facility (SECUF).

AUTHOR DECLARATIONS
Conflict of Interest

The authors have no conflicts to disclose.

Author Contributions

Wenxiao Shi and Jing Zhang contributed equally to this work.

Wenxiao Shi: Investigation (lead); Methodology (lead); Software (lead); Validation (lead); Visualization (lead); Writing – original draft (equal). **Jing Zhang:** Funding acquisition (supporting); Methodology (equal); Software (equal). **Xiaozhi Zhan:** Investigation (equal); Methodology (equal); Validation (equal). **Jialiang Li:** Investigation (supporting); Methodology (supporting); Validation (supporting). **Zhe Li:** Investigation (supporting). **Jie Zheng:** Investigation (supporting). **Mengqin Wang:** Investigation (supporting). **Jine Zhang:** Investigation (supporting). **Hui Zhang:** Investigation (supporting). **Tao Zhu:** Investigation (equal); Methodology (equal); Software (equal); Validation (equal); Writing – review & editing (equal). **Yunzhong Chen:** Funding acquisition (supporting); Supervision (supporting); Writing – review & editing (supporting). **Fengxia Hu:** Funding acquisition (equal); Supervision (supporting); Writing – review & editing (supporting). **Baogen Shen:** Funding acquisition (lead); Supervision (supporting); Writing – review & editing (supporting). **Yuansha Chen:** Conceptualization (lead); Investigation (equal); Methodology (equal); Project administration (lead); Software (supporting); Supervision (lead); Validation (lead); Visualization (equal); Writing – original draft (lead); Writing – review & editing (equal). **Jirong Sun:** Data curation (lead); Funding acquisition (lead); Project administration (lead); Supervision (lead); Validation (equal); Writing – review & editing (lead).

DATA AVAILABILITY

The data that support the findings of this study are available from the corresponding authors upon reasonable request.

REFERENCES

[1]H. Takagi and H. Y. Hwang, Science **327**, 1601–1602 (2010).
[2]M. Imada, A. Fujimori, and Y. Tokura, Rev. Mod. Phys. **70**, 1039–1263 (1998).
[3]E. Dagotto, Science **309**, 257–262 (2005).
[4]Y. Tokura and N. Nagaosa, Science **288**, 462–468 (2000).
[5]J. Heber, Nature **459**, 28–30 (2009).
[6]G. R. Stewart, Rev. Mod. Phys. **73**, 797–855 (2001).
[7]J. M. De Teresa, A. Barthelemy, A. Fert, J. P. Contour, F. Montaigne, and P. Seneor, Science **286**, 507–509 (1999).
[8]S. Okamoto and A. J. Millis, Nature **428**, 630–633 (2004).
[9]P. Yu, J. S. Lee, S. Okamoto, M. D. Rossell, M. Huijben, C. H. Yang, Q. He, J. X. Zhang, S. Y. Yang, M. J. Lee, Q. M. Ramasse, R. Erni, Y. H. Chu, D. A. Arena, C. C. Kao, L. W. Martin, and R. Ramesh, Phys. Rev. Lett. **105**, 027201 (2010).
[10]J. Matsuno, K. Ihara, S. Yamamura, H. Wadati, K. Ishii, V. V. Shankar, H.-Y. Kee, and H. Takagi, Phys. Rev. Lett. **114**, 247209 (2015).
[11]J. Matsuno, N. Ogawa, K. Yasuda, F. Kagawa, W. Koshibae, N. Nagaosa, Y. Tokura, and M. Kawasaki, Sci. Adv. **2**, e1600304 (2016).
[12]X. Liu, W. J. Song, M. Wu, Y. B. Yang, Y. Yang, P. P. Lu, Y. H. Tian, Y. W. Sun, J. D. Lu, J. Wang, D. Y. Yan, Y. G. Shi, N. X. Sun, Y. Sun, P. Gao, K. Shen, G. Z. Chai, S. P. Kou, C. W. Nan, and J. X. Zhang, Nat. Commun. **12**, 5453 (2021).
[13]S. W. Zeng, X. M. Yin, C. J. Li, C. S. Tang, K. Han, Z. Huang, Y. Cao, L. E. Chow, D. Y. Wan, Z. T. Zhang, Z. S. Lim, C. Z. Diao, P. Yang, A. T. S. Wee, S. J. Pennycook, and A. Ariando, Nat. Commun. **13**, 743 (2022).
[14]H. Y. Hwang, S.-W. Cheong, N. P. Ong, and B. Batlogg, Phys. Rev. Lett. **77**, 2041 (1996).
[15]J. Z. Sun, D. W. Abraham, R. A. Rao, and C. B. Eom, Appl. Phys. Lett. **74**, 3017 (1999).
[16]L. F. Kourkoutisa, J. H. Song, H. Y. Hwang, and D. A. Muller, Proc. Natl. Acad. Sci. U. S. A. **107**, 11682 (2010).
[17]Z. Liao, N. Gauquelin, R. J. Green, S. Macke, J. Gonnissen, S. Thomas, Z. Zhong, L. Li, L. Si, S. Van Aert, P. Hansmann, K. Held, J. Xia, J. Verbeeck, G. Van Tendeloo, G. A. Sawatzky, G. Koster, M. Huijben, and G. Rijnders, Adv. Funct. Mater. **27**, 1606717 (2017).
[18]A. Tebano, C. Aruta, S. Sanna, P. G. Medaglia, G. Balestrino, A. A. Sidorenko, R. De Renzi, G. Ghiringhelli, L. Braicovich, V. Bisogni, and N. B. Brookes, Phys. Rev. Lett. **100**, 137401 (2008).
[19]M. B. Lepetit, B. Mercey, and C. Simon, Phys. Rev. Lett. **108**, 087202 (2012).
[20]Y. Chen, X. Yuan, S. Shan, C. Zhang, R. Liu, X. Zhang, W. Zhuang, Y. Chen, Y. Xu, R. Zhang, and X. Wang, ACS Appl. Mater. Interfaces **14**, 39673–39678 (2022).
[21]H. Boschker, J. Verbeeck, R. Egoavil, S. Bals, G. van Tendeloo, M. Huijben, E. P. Houwman, G. Koster, D. H. A. Blank, and G. Rijnders, Adv. Funct. Mater. **22**, 2235 (2012).
[22]T. T. Fister, D. D. Fong, J. A. Eastman, P. M. Baldo, M. J. Highland, P. H. Fuoss, K. R. Balasubramaniam, J. C. Meador, and P. A. Salvador, Appl. Phys. Lett. **93**, 151904 (2008).
[23]J. S. Lee, D. A. Arena, P. Yu, C. S. Nelson, R. Fan, C. J. Kinane, S. Langridge, M. D. Rossell, R. Ramesh, and C. C. Kao, Phys. Rev. Lett. **105**, 257204 (2010).
[24]N. Mottaghi, R. B. Trappen, S. Y. Sarraf, M. S. Seehra, and M. B. Holcomb, J. Alloys Compd. **826**, 154200 (2020).
[25]N. Mottaghi, R. B. Trappen, S. Kumari, C.-Y. Huang, S. Yousefi, G. B. Cabrera, M. Aziziha, A. Haertter, M. B. Johnson, M. S. Seehra, and M. B. Holcomb, J. Phys. Condens. Matter **30**, 405804 (2018).
[26]Z. Liao, F. Li, P. Gao, L. Li, J. Guo, X. Pan, R. Jin, E. W. Plummer, and J. Zhang, Phys. Rev. B **92**, 125123 (2015).
[27]P. Bruno, Phys. Rev. B **39**, 865–868 (1989).
[28]P. Bruno, KFA Jülich:Jülich pp. 24.1–28 (1993).
[29]C. L. Teske and H. Mueller-Buschbaum, Z. Anorg. Allg. Chem. **379**, 234–241 (1970).
[30]D. P. Norton, B. C. Chakoumakos, J. D. Budai, D. H. Lowndes, B. C. Sales, J. R. Thompson, and D. K. Christen, Science **265**, 2074–2077 (1994).
[31]D. Samal, H. Tan, H. Molegraaf, B. Kuiper, W. Siemons, S. Bals, J. Verbeeck, G. Van Tendeloo, Y. Takamura, E. Arenholz, C. A. Jenkins, G. Rijnders, and G. Koster, Phys. Rev. Lett. **111**, 096102 (2013).
[32]Z. Liao, E. Skoropata, J. W. Freeland, E.-J. Guo, R. Desautels, X. Gao, C. Sohn, A. Rastogi, T. Z. Ward, T. Zou, T. Charlton, M. R. Fitzsimmons, and H. N. Lee, Nat. Commun. **10**, 589 (2019).
[33]Z. C. Zhong, G. Koster, and P. J. Kelly, Phys. Rev. B **85**, 121411 (2012).
[34]S. Bhatti, R. Sbiaa, A. Hirohata, H. Ohno, S. Fukami, and S. N. Piramanayagam, Mater. Today **20**, 530 (2017).
[35]S. Ikeda, K. Miura, H. Yamamoto, K. Mizunuma, H. D. Gan, M. Endo, S. Kanai, J. Hayakawa, F. Matsukura, and H. Ohno, Nat. Mater. **9**, 721 (2010).
[36]L. Q. Liu, C. F. Pai, Y. Li, H. W. Tseng, D. C. Ralph, and R. A. Buhrman, Science **336**, 555 (2012).
[37]S. Emori, U. Bauer, S. M. Ahn, E. Martinez, and G. S. D. Beach, Nat. Mater. **12**, 611 (2013).
[38]N. P. Armitage, P. Fournier, and R. L. Greene, Rev. Mod. Phys. **82**, 2421–2487 (2010).
[39]M. T. Johnson, P. J. H. Bloemen, F. J. A. denBroeder, and J. J. deVries, Rep. Prog. Phys. **59**, 1409 (1996).
[40]I. K. Schuller, S. Kim, and C. Leighton, J. Magn. Magn. Mater. **200**, 571 (1999).
[41]B. Dieny and M. Chshiev, Rev. Mod. Phys. **89**, 025008 (2017).
[42]M. R. Fitzsimmons, S. D. Bader, J. A. Borchers, G. P. Felcher, J. K. Furdyna, A. Hoffmann, J. B. Kortright, I. K. Schuller, T. C. Schulthess, S. K. Sinha, M. F. Toney, D. Weller, and S. Wolf, J. Magn. Magn. Mater. **271**, 103–146 (2004).

20 June 2024 09:12:49

[43] J. Li, M.-X. Guan, P.-F. Nan, J. Wang, B.-H. Ge, K.-M. Qiao, H.-R. Zhang, W.-H. Liang, J.-Z. Hao, H.-B. Zhou, F.-R. Shen, F.-X. Liang, C. Zhang, M. Liu, S. Meng, T. Zhu, F.-X. Hu, T. Wu, J. D. Guo, J. R. Sun, and B. G. Shen, Nano Energy **78**, 105215 (2020).

[44] S. Li, Q. Zhang, S. Lin, X. Sang, R. F. Need, M. A. Roldan, W. Cui, Z. Hu, Q. Jin, S. Chen, J. Zhao, J. Wang, J. Wang, M. He, C. Ge, C. Wang, H. Lu, Z. Wu, H. Guo, X. Tong, T. Zhu, B. Kirby, L. Gu, K. Jin, and E. Guo, Adv. Mater. **33**, 2001324 (2021).

[45] Q. Jin, Z. Wang, Q. Zhang, Y. Yu, S. Lin, S. Chen, M. Qi, H. Bai, A. Huon, Q. Li, L. Wang, X. Yin, C. S. Tang, A. T. S. Wee, F. Meng, J. Zhao, J. Wang, H. Guo, C. Ge, C. Wang, W. Yan, T. Zhu, L. Gu, S. A. Chambers, S. Das, T. Charlton, M. R. Fitzsimmons, G. Liu, S. Wang, K. Jin, H. Yang, and E. Guo, Phys. Rev. Lett. **128**, 017202 (2022).

[46] S. Valencia, Z. Konstantinovic, D. Schmitz, A. Gaupp, L. Balcells, and B. Martinez, Phys. Rev. B **84**, 024413 (2011).

[47] D. Pesquera, G. Herranz, A. Barla, E. Pellegrin, F. Bondino, E. Magnano, F. Sanchez, and J. Fontcuberta, Nat. Commun. **3**, 1189 (2012).

[48] F. M. F. de Groot, J. C. Fuggle, B. T. Thole, and G. A. Sawatzky, Phys. Rev. B **41**, 928 (1990).

[49] C. Aruta, G. Ghiringhelli, A. Tebano, N. G. Boggio, N. B. Brookes, P. G. Medaglia, and G. Balestrino, Phys. Rev. B **73**, 235121 (2006).

[50] A. K. Jaiswal, D. Wang, V. Wollersen, R. Schneider, M. L. Tacon, and D. Fuchs, Adv. Mater. **34**, 2109163 (2022).

[51] Z. Cui, A. J. Grutter, H. Zhou, H. Cao, Y. Dong, D. A. Gilbert, J. Wang, Y.-S. Liu, J. Ma, Z. Hu, J. Guo, J. Xia, B. J. Kirby, P. Shafer, E. Arenholz, H. Chen, X. Zhai, and Y. Lu, Sci. Adv. **6**, eaay0114 (2020).

20 June 2024 09:12:49